Earth Planet. Sci. Lett. 655 (2025) 119245

Contents lists available at ScienceDirect

Earth and Planetary Science Letters

journal homepage: www.elsevier.com/locate/epsl

Lower crustal thickening drives active uplift in Northern Tibet

Shaozhuo Liu[a,b,c,*], Xiwei Xu[d,*], Jean-Mathieu Nocquet[c,e], Guihua Chen[a], Xibin Tan[f], Sigurjón Jónsson[b], Yann Klinger[c]

[a] State Key Laboratory of Earthquake Dynamics, Institute of Geology, China Earthquake Administration, Beijing 100029, PR China
[b] Physical Science and Engineering Division, King Abdullah University of Science and Technology, Thuwal, Makkah 23955, Saudi Arabia
[c] Université de Paris, Institut de physique du globe de Paris, CNRS, F-75005 Paris, France
[d] School of Earth Sciences and Resources, China University of Geosciences (Beijing), Beijing 100083, PR China
[e] Geoazur, IRD, Université Côte d'Azur, CNRS, Observatoire de la Côte d'Azur, Valbonne 06560, France
[f] Key Laboratory of Mountain Hazards and Surface Processes, Institute of Mountain Hazards and Environment, Chinese Academy of Sciences, Chengdu 610041, PR China

ARTICLE INFO

Keywords:
Tectonic uplift
Surface processes
Lower crustal thickening
East Kunlun Shan mountain range
Tibetan plateau

ABSTRACT

Mountains in collisional orogens generally grow as crustal rocks are advected over low-angle thrust faults, suggesting a close relationship between tectonic uplift and upper crustal shortening. For example, the Himalayas, hosting large-scale thrust fault systems, undergoes ~15–20 mm/year shortening and concomitant ~5 mm/year active uplift. However, geodetic observations reveal an active uplift of 1–2 mm/year across the East Kunlun Shan mountain range, the northern margin of the Tibetan Plateau, where no active thrust fault has been identified. This active uplift is too fast to be explained by the limited horizontal shortening of at most 1.0 ± 0.2 mm/year. After quantifying and correcting for contributions arising from erosion, (de)glaciation, and recent earthquakes, the uplift rate across the East Kunlun Shan still amounts to 1.0 ± 0.5 mm/year. Our simulations show that mantle processes cannot explain the GPS-observed uplift. We find that lower crustal thickening, rather than upper crustal shortening alone, drives the ongoing uplift across the East Kunlun Shan, hence challenging our current views on mountain range dynamics.

1. Introduction

Whether the present-day 5-km-high Tibetan Plateau continues to rise remains unknown (Kapp and DeCelles, 2019; Ding et al., 2022). The Tibetan Plateau has been largely elevated by crustal shortening and thickening and is continuously modified by surface processes and subsurface geodynamic processes (England and Houseman, 1988; Molnar et al., 1993; Yin and Harrison, 2000; Tapponnier et al., 2001; Kapp and DeCelles, 2019; Ding et al., 2022). However, crustal extension and thinning have been ongoing since the middle Miocene (Armijo et al., 1986; Blisniuk et al., 2001; Taylor et al., 2003; Shapiro et al., 2004; Elliott et al., 2010; Styron et al., 2015; Wang and Shen, 2020), potentially leading to ~1 km elevation drop (Molnar et al., 1993; Ge et al., 2015) and ongoing subsidence (Wang and Barbot, 2023) in central Tibet (Fig. 1). In adjacent regions, elevation gain might occur where crustal thrust-wedges grow laterally and vertically along with oblique lithospheric mantle subduction (Tapponnier et al., 2001) or where influx of lower crustal material thickens the crust (Clark et al., 2005; Royden et al., 2008). These inferences are mainly based on long-term fault slip and topography and short-term physical properties of the Earth's interior, as direct evidence from short-term active deformation are rare. To gain more insights into the dynamics of plateau evolution, accurate observations of active deformation are needed across specific tectonic transition zones within the Tibetan Plateau (Kapp and DeCelles, 2019; Ding et al., 2022), such as the ~5-km-elevation East Kunlun Shan (EKS) mountain range (Fig. 1).

The EKS, stretching east to west for ~1000 km, divides the 4–5-km-elevation Hoh Xil Basin and ~2.8-km-elevation Qaidam Basin which were hypothesized to be a continuous topographic low referred to as the Paleo-Qaidam basin (Yin et al., 2008; Kapp and DeCelles, 2019; Ding et al., 2022). Paleozoic granitoids are extensively exposed on the EKS, while the region to the south is covered by thick Triassic turbidites (e.g., Wu et al., 2019) and the Qaidam Basin to the north is covered by Cenozoic sediments of about 10 km in thickness (e.g., Yin et al., 2008). Along with these variations in topography and surface geology, there are notable differences in lithospheric structure across the EKS. The crust is

* Corresponding authors.
E-mail addresses: shaozhuo.liu@kaust.edu.sa (S. Liu), xiweixu@vip.sina.com (X. Xu).

https://doi.org/10.1016/j.epsl.2025.119245
Received 9 May 2024; Received in revised form 13 November 2024; Accepted 31 January 2025
Available online 12 February 2025

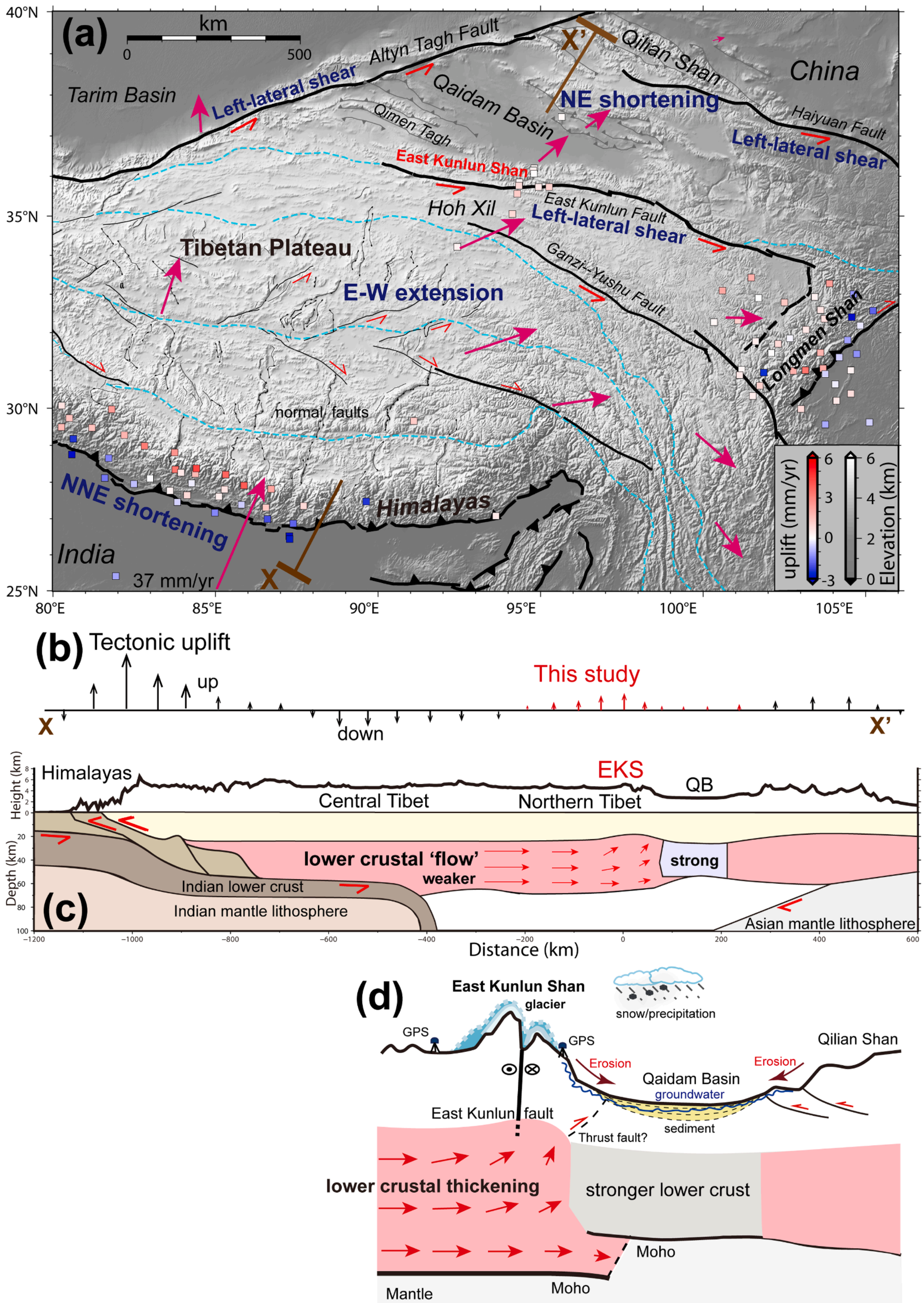

Fig. 1. Tectonic setting of the Tibetan Plateau and climate-tectonic system at the East Kunlun Shan. (a) Superimposed on the shaded-relief topography are crustal motions (magenta vectors) with respect to the stable Eurasia (Wang and Shen, 2020), active strike-slip (black lines with red half arrows), normal (black lines with squares), thrust faults (black and gray lines with triangles), suture zones (dashed cyan lines), and GPS-observed uplift across the East Kunlun Shan (this study), Longmen Shan (Wang et al., 2021), and Himalayas (Fu and Freymueller, 2012). (b) Possible patterns of present-day tectonic uplift (red vectors are our new results; black are the model-extrapolated (Wang and Barbot, 2023), which are built on limited campaign GPS measurements on the high plateau) along the N30°E-directed X-X' profile as shown in (a). (c) Schematic cross-section of the Tibetan Plateau along the N30°E-directed X-X' profile. (d) Schematic diagram showing the key elements of the climate-tectonic system: topography, major faults, glaciers, sediment, erosion, precipitation, groundwater, and a weaker lower crust beneath the plateau subjected to lower crustal thickening.

about 50 km thick (e.g., Karplus et al., 2011) and the lithosphere, including the lower crust, is exceptionally strong on the Qaidam Basin side (e.g., Jordan and Watts, 2005). In contrast, the region to the south of the EKS has a 70 km thick crust and a weaker lower crust (e.g., Karplus et al., 2011; Ryder et al., 2011). The EKS perhaps began to rise in the Oligocene (Yin et al., 2008; Kapp and DeCelles, 2019; Ding et al., 2022) and then experienced significant uplift (Yin et al., 2008; Li et al., 2021; Ding et al., 2022), possibly reaching an elevation of over 4 km after the middle Miocene (Ding et al., 2022). However, whether the EKS continues to rise has remained unknown (e.g., Wang and Barbot, 2023). Its present-day tectonics is dominated by left-lateral strike-slip faulting along the E-W striking East Kunlun fault (EKF) (Wang and Shen, 2020), with a Holocene left-lateral slip rate of 12.1 $\pm$ 2.6 mm/yr (Van der Woerd et al., 1998). This Cenozoic fault activity is associated with reactivation of a pre-existing weakness along the Triassic Kunlun suture (e.g., Yin and Harrison, 2000). The onset time of this Cenozoic faulting remains debated (Jolivet et al., 2003; Duvall et al., 2013), possibly, in the late Oligocene or in the early Miocene (Duvall et al., 2013; Staisch et al., 2020), coinciding with the end of appreciable north-south upper crustal shortening in the Hoh Xil (Yin et al., 2008; Clark et al., 2010; Staisch et al., 2016). Hence, the current regional tectonics may not allow building major topography across the EKS.

This study aims to unravel the physical processes, both on the Earth's surface and within its interior, that drive the decadal-scale vertical motion observed by Global Positioning System (GPS) measurements across the EKS near 93.0°−95.5°E longitude. In Section 2, we present the GPS-derived shortening and vertical rates across the EKS, highlighting the presence of active uplift in the context of limited shortening rate. Since vertical motions result from tectonic, geodynamic, and non-tectonic processes, in Section 3 and 4, we quantify the perturbations from recent earthquakes and surface processes, along with the contributions from other tectonic and geodynamic sources. In Section 5, we discuss the mechanisms potentially driving this active uplift. We find that the EKS continues to rise with respect to the adjacent central Tibet and Qaidam Basin, as a passive response to the northward transport of the Tibetan lower-crustal material that is impeded by the mechanically stronger Qaidam Basin.

2. Sharp uplift gradient across the East Kunlun Shan

Since 2007, we have collected continuous GPS measurements at 11 stations anchored into the bedrock outcrops across the EKS (Fig. 2 and Fig. S1; Text S1). We process these GPS observations using GAMIT/GLOBK (release 10.71) (Herring et al., 2017). Our GPS position time series (Fig. S1) are expressed in the International Terrestrial Reference Frame 2014 (ITRF2014) (Altamimi et al., 2016). We focus on the uplift at the EKS and its surroundings with respect to the Qaidam Basin (Text S2). We correct the GPS position time series for regional common mode error (Text S3) and account for time-correlated noise when estimating the 3D velocities at the GPS stations (Text S4).

Our data, combined with published 2D horizontal velocities (Wang and Shen, 2020), provide 3D present-day crustal deformation across the EKS at a precision of a few tenths of millimeter per year. We inferred ~8 mm/yr left-lateral shear across the East Kunlun Fault (EKF) which was essentially locked before the 2001 Mw7.8 Kokoxili earthquake (Liu et al., 2019). The adjustment of the Earth's crust and mantle following the 2001 earthquake rupture generated an additional ~10 mm/yr asymmetric left-lateral shear across the EKF during the 2007–2016 period (Liu et al., 2019). Also, GPS horizontal velocities indicate at most ~1.0 $\pm$ 0.2 mm/yr shortening rate smoothly varying across the EKF before the 2001 event (Fig. 2b). However, the GPS vertical rates show a ~200-km-wide zone of asymmetric uplift and highlight a sharp gradient of 1–2 mm/yr over ~50 km between the Qaidam Basin and the EKS where the maximum vertical rate is observed (Fig. 2c).

3. Modeling method

Vertical motions on the Earth's surface are the Solid Earth's response to several processes, including tectonic, geodynamic, and surface processes (e.g., Hammond et al., 2021). Here, we use geophysical models to quantify 1) the interseismic deformation associated with fault slip, 2) the postseismic deformation caused by recent large earthquakes, 3) the solid Earth's response to multi-time-scale surface mass redistribution (mainly of climate-related origin), 4) the uplift caused by lower crustal thickening, and 5) the uplift caused by mantle processes. We assess both the model-predicted magnitude of vertical rates and their ability to explain the GPS-observed uplift pattern, aiming to obtain reliable constraints on the actual vertical uplift rates driven by tectonic processes.

3.1. Modeling interseismic deformation caused by fault slip

We first evaluate the strain partitioning caused by strain accumulation on the East Kunlun fault (EKF) (Fig. S5) and Ganzi-Yushu fault (GYF) (Liu et al., 2019), using dislocation models in an elastic half space (Okada, 1992). After correcting for the contributions from the EKF and GYF, we attempt to explain the GPS-observed horizontal and vertical rates using a simple ramp and flat décollement model based on elastic dislocation theory (Okada, 1992). For simplicity, we consider two representative ramp-flat thrust models, one dipping toward the north (e.g., Shi et al., 2009; Wang et al., 2011) and the other toward south (e.g., Tapponnier et al., 2001); the shallower portion of fault ramp is assumed to be locked; the reverse-slip rate on the ramp is determined by its dip to keep consistent with the shortening on the flat décollement. We use a grid-search approach to find the optimal locking depth, dip angle, slip rate, width, and position of the surface trace of the ramp, minimizing the misfit between the 3D GPS velocities and model prediction. In this optimization, the 1-sigma uncertainties are amplified to 0.8 mm/yr for the campaign GPS horizontal velocities (Wang and Shen, 2020).

3.2. Modeling postseismic transients

We evaluate how the postseismic transients following the 2001 Mw 7.8 Kokoxili earthquake (Ryder et al., 2011; Liu et al., 2019) affected our GPS observations during the 2007–2016 period used in this study. For that purpose, we use the earthquake rupture model (Fig. S6 and Text S5) to drive afterslip (aseismic slip surrounding the rupture and on its down-dip extension) and viscoelastic relaxation (stress adjustment to earthquake-induced stress loading in the ductile lower crust and upper mantle). We consider afterslip governed by rate-strengthening friction (Barbot et al., 2009). To simulate viscoelastic relaxation, we use PyLith (Aagaard et al., 2013) and considered a Burgers Body rheology which is composed of a Maxwell element in series with a Kelvin element. For simplicity, 1) the Kelvin (transient) viscosity is an order of magnitude lower than the Maxwell ("steady-state") viscosity; 2) we set the Maxwell viscosity as 2–4 $\times$ 10^{19} Pa s for the lower crust to the south of the basin margin (Wen et al., 2012; Liu et al., 2019; Zhao et al., 2021); 3) using a grid-search approach that minimizes the misfit between the 3D GPS time series and model predictions, we estimate the lateral contrast in the lower crustal viscosity and the crust-to-mantle viscosity ratio.

3.3. Modeling elastic and viscous uplift caused by climate-related surface processes

Following the approach tested for the New Zealand's Southern Alps (Liu et al., 2024), we use elastic and viscoelastic load deformation models to evaluate the solid Earth's response to multi-time-scale surface processes that result in mass redistribution on the Earth's surface (Text S7-S8). In all the load deformation models, the elastic and density structure of the Earth model above 80 km depth are derived from the regional seismic velocity model (Karplus et al., 2011) and follow the PREM model (Dziewonski and Anderson, 1981) below.

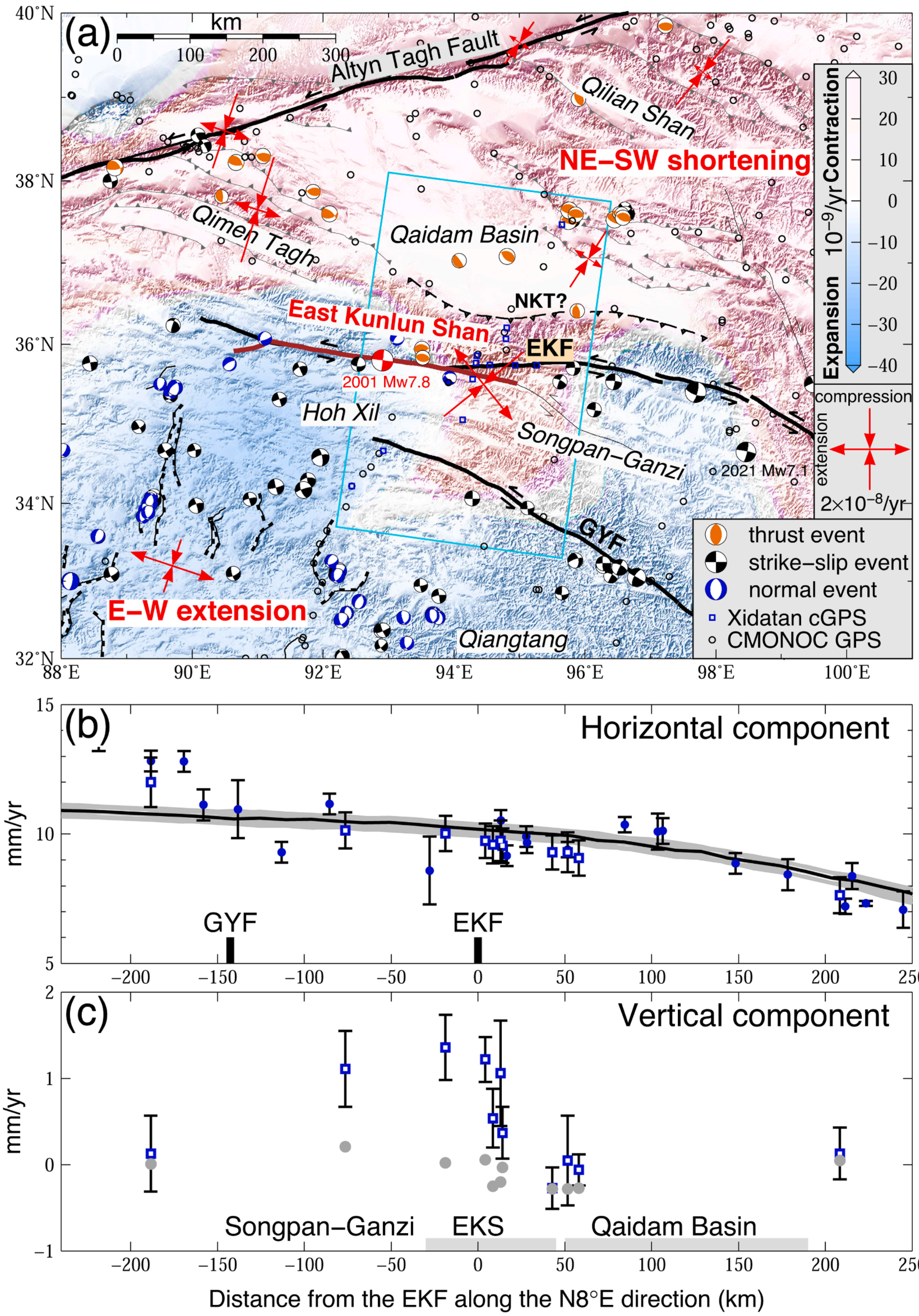

Fig. 2. Areal strain rate and horizontal and vertical GPS velocities across the East Kunlun Shan. (a) GPS-derived contraction and expansion strain rates (background color) and principal strain rates (red vectors) (Wang and Shen, 2020). Also shown are active strike-slip (black lines), normal (black lines with squares), and thrust faults (black lines with triangles), focal mechanisms for the M > 4 events during 1976–2021 (beach balls; https://www.globalcmt.org/), the surface trace of the 2001 Mw7.8 Kokoxili earthquake (brown line), and locations of GPS stations (open circles and squares). (b) Horizontal GPS velocities before the 2001 event in the N8°E direction (with 1-sigma error bars) within a ~300-km-wide swath (cyan rectangle in (a)) from our Xidatan continuous and CMONOC (Wang and Shen, 2020) GPS networks. Solid black line shows interpolated shortening rate (Shen et al., 2015), with the 1-sigma uncertainties in gray shade, along the center of the swath. (c) Vertical GPS rates (blue symbols with 1-sigma uncertainties) at our Xidatan GPS stations. Gray dots show the perturbation during 2007–2016 from models of postseismic deformation following the 2001 Mw7.8 Kokoxili event.

We evaluate the solid Earth's elastic response to present-day glacier retreat and hydrological loading, based on elastic loading theory (Farrell, 1972; Chen et al., 2017a), with ~1-km spatial resolution (Fig. S10).

We evaluate the (de)glaciation-induced viscoelastic deformation—-glacial isostatic adjustment (GIA)—using an approach based on spherical harmonics and viscoelastic Load Love numbers (Spada et al., 2011; Melini et al., 2022). The earth structure has 5 major layers: an effectively elastic lid, the lower crust plus the lithospheric upper mantle above 200 km depth, 470-km-thick deep upper mantle (200–410 km depth) and transition zone (410–670 km depth), 2231-km-thick lower mantle, and the fluid core. About the elastic lid, we consider two representative elastic shell thicknesses, 20 and 50 km, bracketing the plausible range found by gravity data for Northern Tibet (Jordan and Watts, 2005). This elastic thickness reflects the long-term response to topographic loading and should be lower than the apparent elastic thickness for decadal-centennial-millennial-scale (un)loading (Watts et al., 2013; Lau et al., 2021). To mimic the elastic behavior at the relevant time scale using viscoelastic rheology, the elastic lid was set to have an effective viscosity of 1×10^{50} Pa s. We consider a Burgers rheology for the topmost viscoelastic layer(s) beneath the elastic lid when modeling the GIA associated with the Little Ice Age (LIA), unless otherwise specified (Fig. S11-S20). However, we used a simple Maxwell rheology to model the Last Glacial Period (LGP) GIA, as the steady-state rheology governs the ongoing uplift driven by (de)glaciation about 10 kyr ago (Fig. S21-S24). All the details are presented in Text S9.

The Load Love numbers for incompressible and self-gravitating Earth model were computed in the center of mass of the solid Earth frame up to a maximum spherical harmonic degree of 2000/1000 for the LIA/LGP GIA. The truncated harmonic degree of 2000 guarantees enough precision for modeling near-field viscous deformation. For modeling LGP GIA, after harmonic degree of 1000, the viscous part of Load Love number converges to zero, and only the elastic part is left.

For simplicity, (de)glaciation is assumed to occur synchronously across all the glaciers; inter-decadal (millennial) glaciation fluctuations during the LIA (LGP), even though they had occurred, are not considered, because they are relatively smaller than the main trend(s).

We use a similar assumption while assessing the ongoing vertical motion associated with viscoelastic rebound in response to erosion (Fig. S26) and sedimentation (Fig. S25). The impacts from spatial-temporal variation of erosion and sedimentation are summarized in Text S10.

3.4. Modeling uplift caused by lower crustal thickening

We use the 2D finite element model ADELI (Hassani et al., 1997) to simulate the vertical deformation near the EKS induced by lower crustal thickening driven by the topographic and far-field loading. Because our GPS profile extends above the middle of the low seismic velocity zone (perhaps mechanically weaker) in the lower crust which extends over 800 km from longitude 92°E-101°E (Li et al., 2014), 2D models are acceptable. Our 2D model represents a 1000-km long and N-S trending transect across the EKS. The model geometry (Fig. S27) mimics the first-order variations of topography across the EKS, with 2 km topography on the 500-km-long left portion that is compensated by a crustal root. This length scale is set to avoid spurious deformation near the EKS arising from boundary conditions. Our 2D model is divided into four sub-domains: upper crust, upper mantle, and lower crust beneath the basin and plateau interior.

We use elasto-visco-plastic rheology to simulate the brittle and ductile behavior of the lithosphere, with the failure criterion determined by the Drucker-Prager model (internal friction angle is 15° and the cohesion is 10^7 Pa). Rocks deform elastically, brittlely, or ductily, depending on the local deviatoric stresses, pressure, and temperature. The temperature field approximates the geotherm of Northern Tibet (Jiang et al., 2019): 0 °C temperature and 50×10^{-3} Wm^{-2} heat flow on the surface, 20×10^{-3} Wm^{-2} heat flow at the bottom of lithospheric mantle (~130 km depth). We consider an upper crust with quartz rheology (Carter and Tsenn, 1987) and lower crust with lateral variation in strength by assigning a mafic granulite rheology (Wang et al., 2012) for the plateau side and dry diabase rheology (Mackwell et al., 1998) for the basin side. To confirm the need for lateral variation in lower crustal strength, we also test a case with the same rheology for the lower crust beneath both the plateau and the basin. For simplicity, the upper mantle is assumed to have Maxwell viscosity of 1×10^{25} Pa s, which inhibits convection in the mantle. Also, our model allows for upper crust and mantle decoupling, which is required to explain the GPS-derived uplift. The bottom of our model experiences lithostatic pressure. The right-side boundary is fixed in the horizontal direction but has free slip in the vertical direction. The left side of the lower crust is subjected to horizontal velocity loading of 5, 10, and 15 mm/yr (Fig. S27). We first run our simulation without velocity loading from 0 to 1.0 Ma (the time step is ~1 year), until the velocity essentially remains steady, to deal with the incomplete force balance associated with the lateral density variation. Then, the velocity loading gradually increases to the full 5, 10, and 15 mm/yr in about 0.5 Ma, and the 5, 10, and 15 mm/yr loading continues for about 0.4 Ma. The choice of a timescale of 0.4 Ma is based on two criteria: (1) the model-predicted vertical rate becomes stable for a few tens of millennia, (2) large finite strain (permanent bulking of the crust of the plateau) does not occur.

3.5. Modeling uplift caused by mantle processes

We evaluate how present-day thermal buoyancy in the upper mantle modulates the present-day deformation using ASPECT (Advanced Solver for Planetary Evolution, Convection, and Tectonics) (Kronbichler et al., 2012; Heister et al., 2017; Liu and King, 2019; Euen et al., 2023). The driving force of deformation is the buoyancy resulting from density perturbations ($\delta\rho$, in which ρ is density) due to thermal expansion ($\delta\rho =$ -$\alpha \times \rho \times \delta_T$, in which thermal expansivity, α, is 2×10^{-5} K^{-1} and δ_T is the temperature perturbation). In our simulations, the evolution of topography at spatial scale of 10s-100 s km is influenced by crustal and lithospheric density and thickness variations (e.g., Flament et al., 2013). Since the 3D crustal and lithospheric structure of the entire Tibetan Plateau is still not well constrained, for simplicity, we consider 2D models (1000 km long and ~500 km wide) with topography that mimics the cross-section of the EKS. To ensure consistency with Section 3.4, we consider the same rheological layering for the crust. To include upper-mantle processes, we consider a composite rheology for dry olivine, for which the effective viscosity $\left(\eta_{diff}\eta_{disl} / \left(\eta_{diff} + \eta_{disl}\right)\right)$ is the harmonic average of viscosity from diffusion creep $\left(\eta_{diff}\right)$ and dislocation creep (η_{disl}). The background temperature (T) increases from 273 K on the Earth's surface to 1600 K at the lithosphere-asthenosphere boundary and increases adiabatically by ~0.5 K/km below. The temperature perturbations (δ_T) are converted from the anomaly in shear wave velocity (δlnV_s in Fig. S28, in which V_s is the shear wave velocity) (Chen et al., 2017b), according to the scaling law ($\delta T = -(\xi/\alpha)\delta lnV_s$, in which α is 2.5×10^{-5} and ξ is 0.05 for the upper mantle above 300 km depth), as proposed by Liu and King (2022). Based on these settings, the effective viscosity (Fig. S29) is on the order of 10^{19}–10^{20} Pa s, about 1–2 orders of magnitude lower than the background mantle viscosity, for the uppermost mantle at a depth of 70–120 km where about 3 %–5 % decrease in shear wave velocity was found (Chen et al., 2017b). The bottom of the model is fixed, the left and right boundaries are allowed to have tangential motions, and the top surface is a free surface. We use the "single Advection and iterated Stokes" scheme to solve the partial differential equations governing the deformation. We choose the model-predicted uplift within 20 thousand years to approximate the present-day uplift (Text S11 and Fig. S30-S31).

4. Contributions from earthquakes and surface processes

4.1. Postseismic transients of the 2001 MW 7.8 kokoxili earthquake

We use the three-dimensional GPS position time series in the time period 2007–2016 to constrain the postseismic deformation model that combines afterslip and viscoelastic relaxation (Fig. 3). The viscoelastic relaxation models consistently predict near-field uplift and subsidence at the GPS stations north and south of the eastern part of the 2001 rupture (Fig. 3c), respectively, opposite to the uplift pattern for afterslip

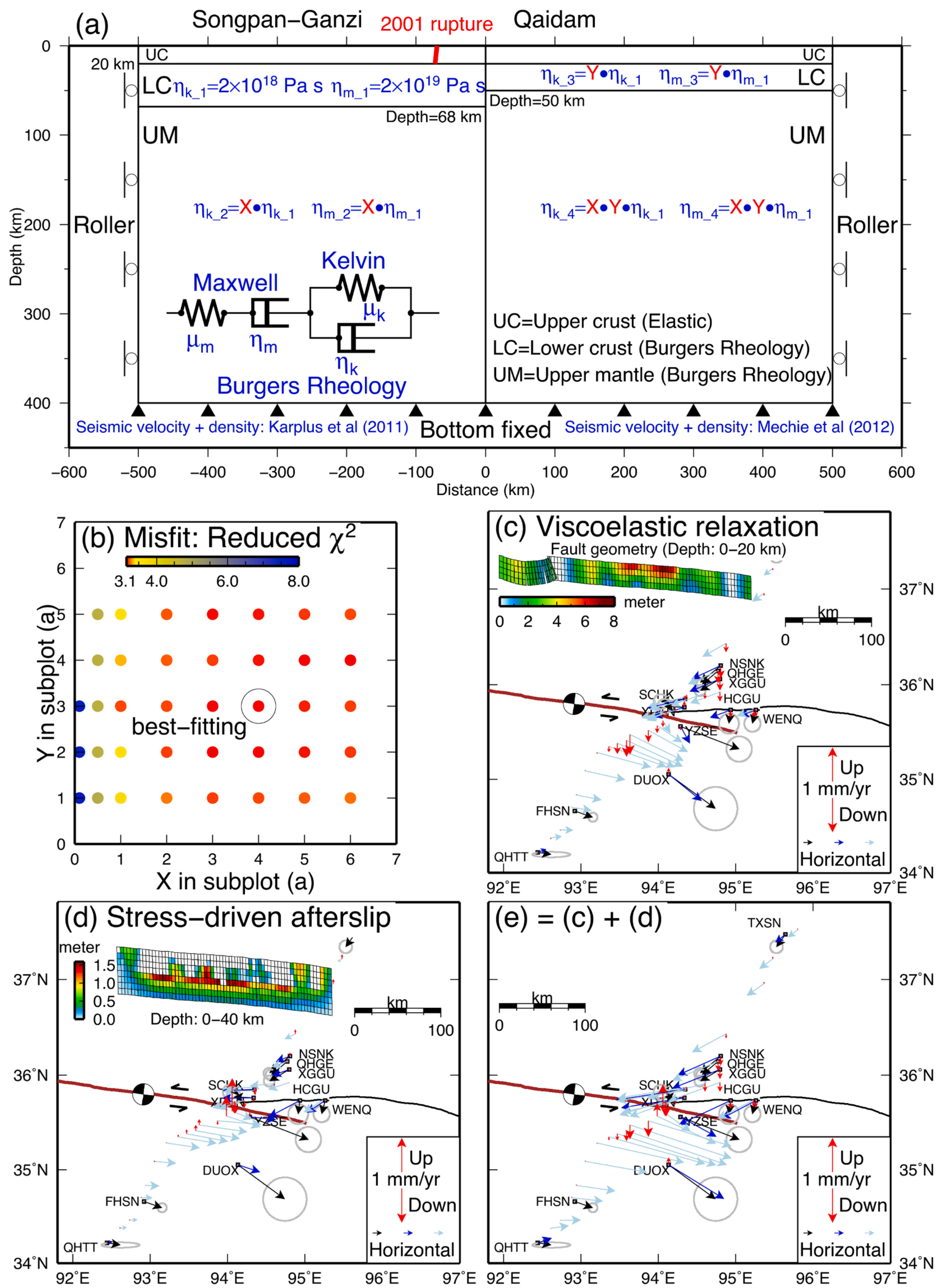

Fig. 3. Postseismic deformation modeling. (a) Finite element model setup for modeling viscoelastic relaxation following the 2001 Mw7.8 Kokoxili earthquake (The model geometry extends 1200 km normal to the cross section. Tetrahedral elements are 1 km close to the earthquake rupture and 5 km in most of the remaining regions). (b) Data misfit (Reduced Chi-square) as a function of X (mantle-to-lower crust viscosity ratio) and Y (lower crustal viscosity lateral contrast), as noted in (a). (c) Observed horizontal (black vectors tipped with 39.3 % confidence error ellipses) and model-predicted horizontal (blue and light blue vectors at the locations of Xidatan continuous and CMONOC campaign GPS stations, respectively) and vertical (red) velocities averaged over the time period 2007–2016 for the best-fit viscoelastic relaxation model. (d) The same as (c), but for stress-drive afterslip. (e) Combined deformation in (c) and (d). Brown lines in (c)-(e) mark the surface trace of the earthquake rupture model. Black squares mark the positions of our Xidatan GPS stations.

(Fig. 3d). These patterns are not well supported by GPS measurements which show that the uplift increases from about 20 km north of the EKF, not at the location of the 2001 rupture (Fig. 1a and Fig. 2c). In the best-fit viscoelastic relaxation model, the upper mantle (Maxwell viscosity greater than 5×10^{19} Pa s) is found to be stiffer than the lower crust beneath the plateau (Maxwell viscosity of 2×10^{19} Pa s), and the limited GPS data on the basin side cannot well resolve the viscosity contrast between the lower crust and upper mantle beneath the basin (Fig. 3a, Fig. 3c). For the time period 2007–2016, viscoelastic relaxation explains 60 %−80 % of the GPS-observed postseismic horizontal deformation in

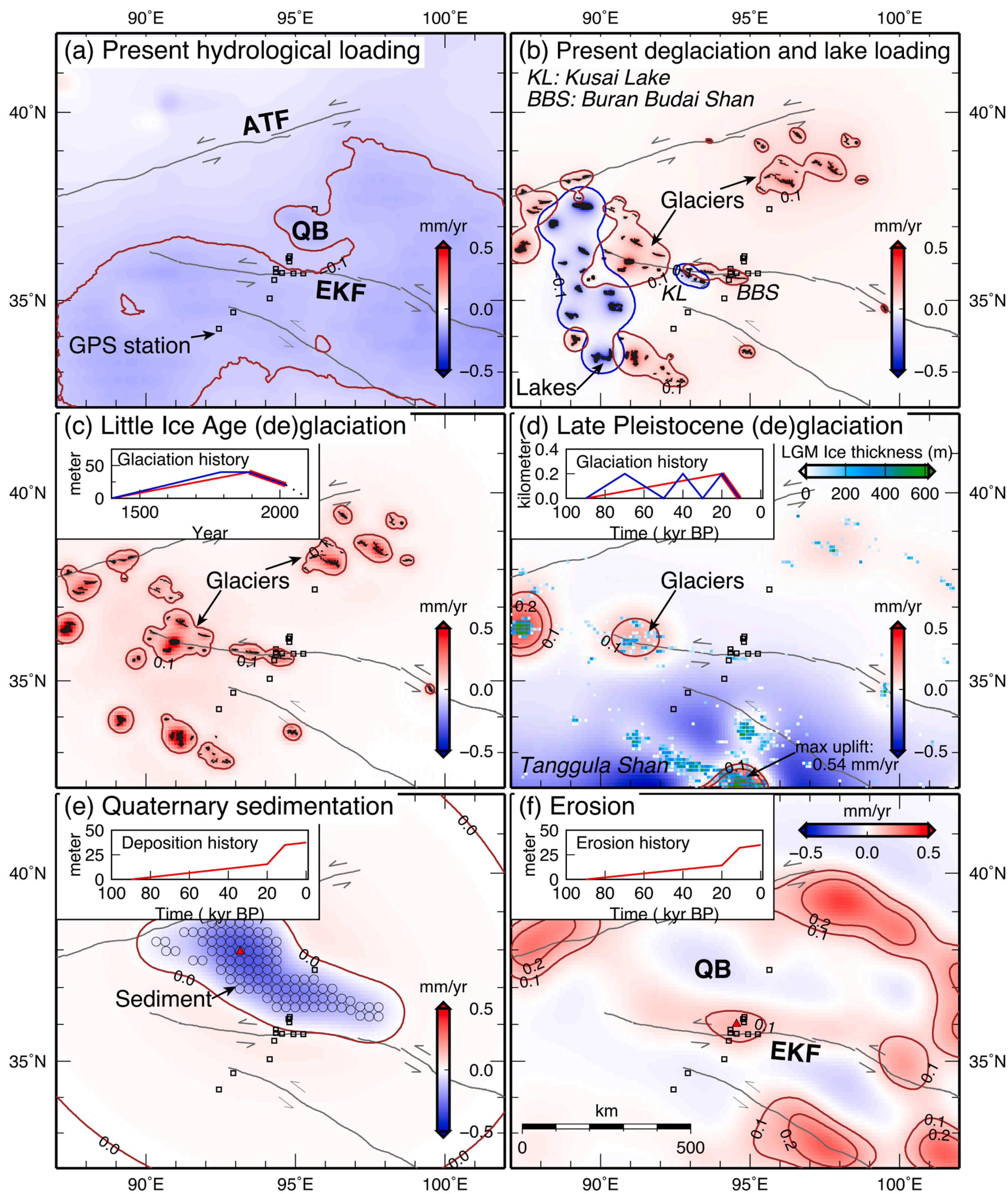

Fig. 4. Present-day vertical motion in response to surface processes. (a) Present hydrological loading by soil moisture and groundwater. (b) Present deglaciation and lake loading. (c) (De)glaciation since the Little Ice Age. (d) Late Pleistocene (de)glaciation. (e) Quaternary sedimentation. (f) Erosion (wind erosion is not considered). (d) to (f) show the maximum vertical motion from the models in which the elastic lid is 20 km thick and upper mantle viscosity is 5×10^{20} Pa s, and, with mantle viscosity below 10^{20} Pa s, the model-predicted vertical motions become even more subtle. Insets in (c) to (f) show the representative loading history (Red and blue curves in the inset (c and d) indicate two representative loading histories, but only the modeling results for the red curves are shown. Red curves in the inset (e and f) show the loading at the positions marked by red triangles in the Qaidam Basin and on the EKS, respectively). The modeling results for the loading histories shown by the blue curves have similar spatial patterns, but the peak amplitude decreases ∼10 % and ∼20 % for (c) and (d), respectively.

the near field south of the 2001 rupture (Fig. 3c), and afterslip explains the remaining 20 %–40 % (Fig. 3d). By increasing the contribution from afterslip, the combined model can reproduce a uplift of 1 mm/yr southward across the 2001 rutpure at the locations of the campaign GPS stations but cannot reproduce the observed uplift pattern at our Xidatan GPS stations. The best-fit combined model shows an uplift gradient of <0.5 mm/yr across the southern Qaidam basin margin during the 2007–2016 GPS observation time window (Fig. 2c and Fig. 3e).

4.2. Elastic and viscous uplift caused by climate-related surface process

Northern Tibet experiences increased precipitation due to global warming (Zhang et al., 2017), which after accounting for evapotranspiration still exerts extra mass load to the solid Earth, causing subsidence that mimics tectonic deformation (Fu and Freymueller, 2012). The elastic rebound due to subsurface hydrological loading, as constrained by the 0.5° × 0.5° resolution WaterGAP groundwater model (Döll et al., 2014) and Climate Prediction Center soil moisture data (Fan and van den Dool, 2004), is 0.1–0.2 mm/yr subsidence around the EKS over the time period 2000–2016 (Fig. 4a). The 0.125° × 0.125° resolution Land Surface Discharge Model, which reflects the terrestrial water (snow, rivers, lakes, and soil moisture) loading (Dill and Dobslaw, 2013), predicts subsidence below 0.05 mm/yr (Fig. S10). Despite variations in accuracy and resolution among the available hydrological data and models (Fig. S10; see Text S7), it is likely that the hydrological loading produces 0.1–0.2 mm/yr elastic subsidence across the EKS (Fig. 4a).

Northern Tibet has mid-sized melting glaciers (Hugonnet et al., 2021) and rising lakes (Zhang et al., 2017), which also drive vertical motions in this region. We consider the elastic response of the crust to current glacier retreat, which is ~0.2 m/yr of reduction in thickness over the last two decades on the EKS (Hugonnet et al., 2021). The model-predicted elastic uplift is locally 0.1–0.2 mm/yr around the modern glaciers on the EKS (Fig. 4b). Thus, the unloading uplift caused by the current glacier retreat is negligible at most GPS stations, except for ~0.1 mm/yr at 4 stations located within 10 km of the glaciers. We also consider the elastic deformation caused by rising lake loading (e.g., the Kusai Lake, ~100 km west of our GPS profile) (Zhang et al., 2017). The model-predicted vertical motion at our GPS stations is negligible, even if the lakes are rising at a maximum rate of ~0.5 m/yr (Zhang et al., 2017).

During the Little Ice Age (LIA, 13th-19th century), modern glaciers advanced by <1 km and thickened by a few tens of meters before shrinking subsequently (Liu et al., 2006; Owen, 2009; Xu and Yi, 2014; Yan et al., 2020; Lee et al., 2021). The adjustment of the Earth's crust and mantle to this ice mass variation causes enduring time-dependent deformation, possibly lasting for at least decades (GIA, glacial isostatic adjustment). We evaluate ongoing uplift caused by GIA since the LIA, based on the published (de)glaciation histories (Fig. 4c) and rheological structures (see Text S9). Our preferred rheological structure has steady-state viscosity of 2–10 × 10^{19} Pa s for the lower crust and lithospheric mantle, based on decadal-scale interseismic (Ge et al., 2022) and postseismic deformation (Ryder et al., 2011; Liu et al., 2019). We set the (de)glaciation histories based on two criteria: half of the LIA ice gain was lost after the LIA, as in the Himalayas case (Lee et al., 2021); and the post-LIA thinning rate before 2000 CE is half of the current glacier retreat, given the accelerated melting since 2000 CE (Hugonnet et al., 2021). Our models suggest isolated patches of ongoing uplift below 0.3 mm/yr around the major modern glaciers (Fig. 4c and Fig. S11-S20). To reproduce our GPS-observed uplift, we need either unrealistically large post-LIA ice thinning over 100 m (a value that only applies to a few spots in the Himalayas (Lee et al., 2021), which had more intense (de)glaciation than the much drier EKS region (Yan et al., 2020; Hugonnet et al., 2021)) or unlikely low effective viscosity (10^{18} Pa s) at the centennial timescale (Fig. S11-S20).

Glacial cycles occurred during the Late Pleistocene (Liu et al., 2006; Owen, 2009), with either one major glacial-deglacial cycle or, alternatively, three shorter cycles during the last glacial period preceding the warm Holocene (Inset in Fig. 4d). Glaciers on the EKS during the Last Glacial Maximum (LGM, about 20 kyr BP) were less extensive than those on the Tanggula Shan (Fig. 4d) and Himalayas (Yan et al., 2018). They were probably ~3–5 times broader and <400 m thicker than the present ones (Yan et al., 2018). Based on these (de)glaciation histories, the GIA models give ongoing subsidence below 0.3 mm/yr at the GPS stations south of the EKS (i.e., far-field subsidence caused by deglaciation along the Himalayas and in Tanggula Shan). The GIA models give negligible uplift across the southern basin margin (Fig. 4d and Fig. S21-S24), irrespective of the tested upper mantle viscosity (10^{19}–10^{21} Pa s). To reproduce our GPS-observed uplift, we need either over 1 km post-LGM ice thinning on the EKS or an extensive thick ice cap fully covering the EKS, both conflicting with the field evidence (Liu et al., 2006; Owen, 2009) and simulated glaciation scenarios (Yan et al., 2018).

Quaternary sedimentation in the Qaidam Basin, ~0.2–0.5 mm/yr averaged over the last ~0.2 Ma (Métivier et al., 1999), might induce ~0.1–0.3 mm/yr ongoing subsidence in the basin (no compaction is considered), while causing negligible ongoing uplift below +0.1 mm/yr across the EKS (Fig. 4e and Fig. S25). Erosion, like any surface mass removal process, causes the solid Earth to rebound where focused erosion has been operating (Fig. 4f). Considering a present-day fluvial erosion rate of <0.5 mm/yr on the EKS (Fig. S9) and 3–10 times faster during the pre-Holocene deglaciation period, plausible erosion-induced present-day uplift is less than +0.2 mm/yr around the EKS and the uplift is <0.1 mm/yr from the basin margin to the EKS (Fig. 4f and Fig. S26).

4.3. Comparison with GPS-observed uplift

In summary, the combined effects of postseismic deformation and vertical motion caused by the isostatic response to erosion, sedimentation, hydrological loading, and (de)deglaciation account for only 0.3–0.5 mm/yr ongoing uplift of the EKS relative to the Qaidam Basin, <40 % of the GPS-observed uplift (Fig. 3, Fig. 4, Fig. 5). Above all, the combined model-predicted ongoing uplift is localized about the small modern glaciers on the EKS, which does not fit the GPS-observed sharp gradient across the basin margin and long-wavelength asymmetry (Fig. 2c).

5. Discussion

5.1. The origin of the East Kunlun Shan uplift

Our continuous GPS measurements highlight ongoing uplift relative to the Qaidam Basin. The uplift of the Qaidam Basin is small at 0.1 ± 0.4 mm/yr relative to stable GPS stations around the Tibetan Plateau. About 0.1 mm/yr of uplift (V_z) requires a shortening strain rate ($\dot{\varepsilon}$) of about 2.7 × 10^{-8}/yr, if a 130-km-thick Qaidam lithosphere thickens uniformly and is close to isostatic equilibrium ($V_z = \dot{\varepsilon} \times \upsilon \times [H_c \times (1 - \rho_c/\rho_a) + H_m \times (1 - \rho_m/\rho_a)]$, in which υ is the Poisson's ratio (0.25), H_c is the thickness of crust (50 km), ρ_c is the density of the crust (2.7 × 10^3 kg/m^3), H_m is the thickness of the lithospheric mantle (80 km), ρ_m is the density of the lithospheric mantle (3.2 × 10^3 kg/m^3), ρ_a is the density of the asthenosphere (3.4 × 10^3 kg/m^3)). This estimate, which includes the contributions from processes in the lower crust and lithospheric mantle, is ~30 %-200 % greater than the present-day shortening strain rate of 1-2 × 10^{-8}/yr (Fig. 2) observed by GPS on the Earth's surface across the basin (Wang and Shen, 2020). In the upper crust, this geodetic estimate of shortening is accommodated by active anticlines (Yin et al., 2008) and by thrust faulting (Elliott et al., 2010) associated with crustal thickening (Shapiro et al., 2004). As the combined contributions of postseismic deformation and surface processes can only explain a small fraction of the observed uplift across the EKS, we therefore conclude that the tectonic uplift of this mountain range amounts to 1.0 ± 0.5 mm/yr (Fig. 1

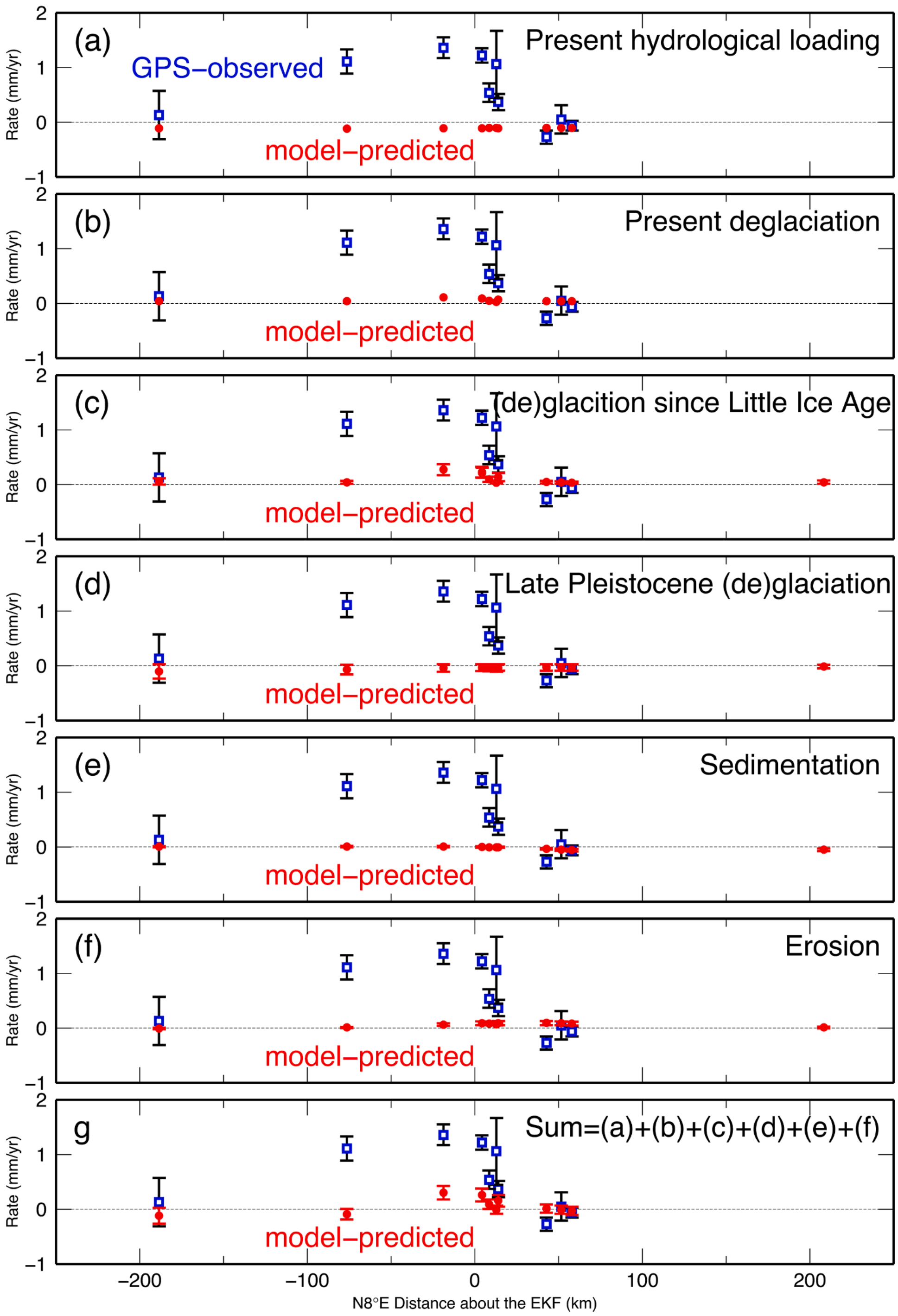

Fig. 5. GPS-observed (blue squares with 1-sigma uncertainties) and model-predicted vertical motions (red dots). Model-predicted elastic deformation caused by (a) Present hydrological loading by soil moisture and groundwater variation and by (b) Present deglaciation and lake loading. Model-predicted viscous deformation caused by (c) (de)glaciation since Little Ice Age, (d) Late Pleistocene (de)glaciation, (e) Quaternary sedimentation, and (f) Erosion. (g) the summation of (a)-(f). The red error bars in (c-f) indicate the minimum and maximum model predictions when the effective viscosity of the shallow upper mantle is greater than or equal to 2×10^{19} Pa s (Fig. S11-S20 and Fig. S21-S26).

and Fig. 5).

One possible explanation for the tectonic uplift is interseismic deformation due to the activity on the thrust faults either dipping toward the north (Shi et al., 2009; Wang et al., 2011) or dipping toward the south (Tapponnier et al., 2001). For the north-dipping case, the best-fit model has a reverse dip-slip rate of ~2.7 mm/yr on a ~32° north-dipping ramp locked above 12 km depth, whose surface trace is about 75–110 km south of the EKF (Fig. 6). The sparsity of GPS uplift rates about 10–100 km south of the EKF does not allow us to conclude the existence of such an active thrust fault (Fig. 7a). For the south-dipping case, reverse slip of ~2.3/1.5 mm/yr on a ~24°/30° south-dipping fault locked above 20 km depth, whose surface trace is close to the suspected Northern Kunlun Thrust (NKT) (Tapponnier et al., 2001), would be needed to explain the GPS-derived uplift (Fig. 2a, Fig. 6, and Fig. 7). However, unless the NKT ruptured recently and earthquake cycle effects are strong, the estimated slip rate is

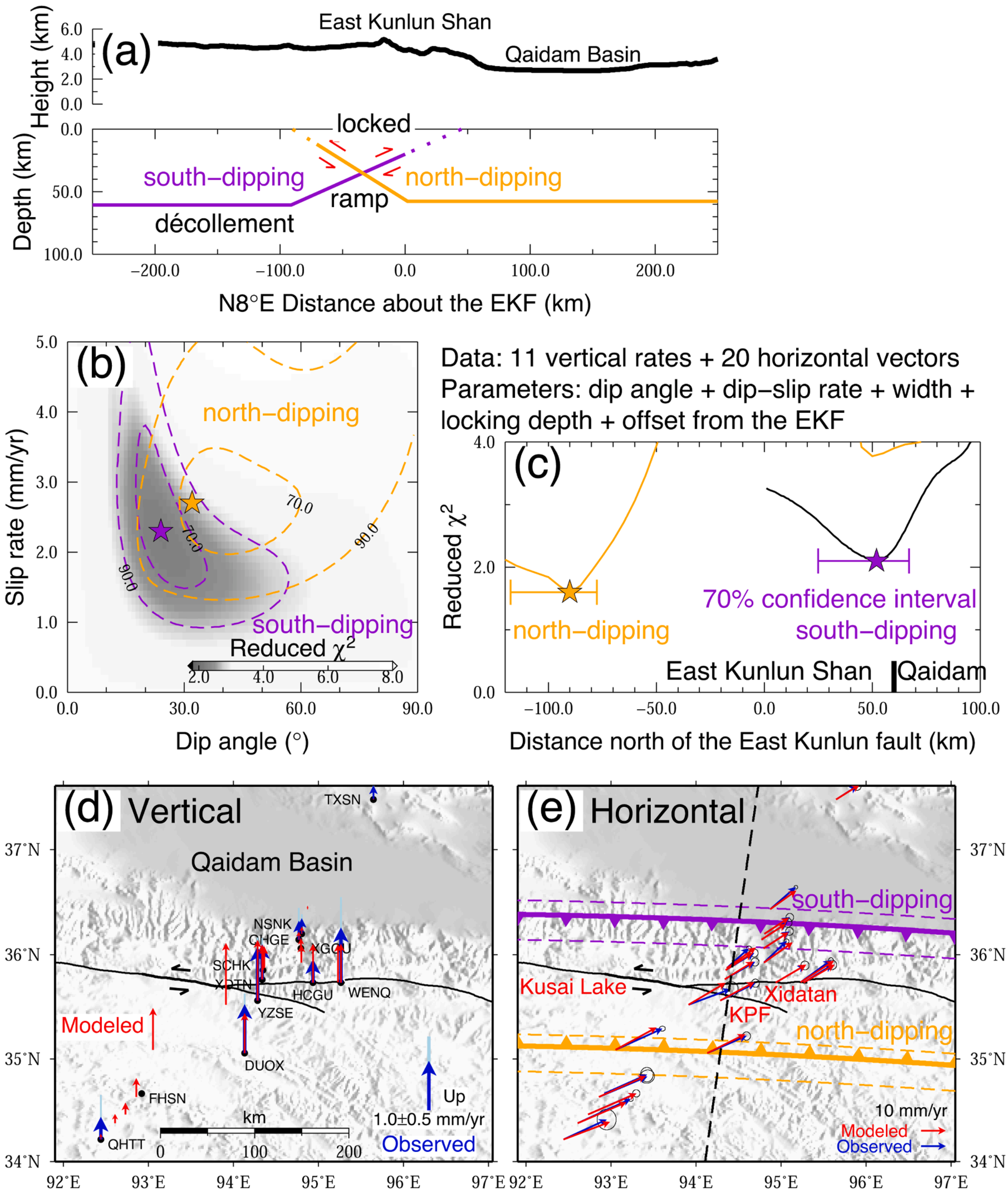

Fig. 6. Dislocation models constrained by the GPS-observed shortening and uplift rates. (a) Topography and ramp-décollement models. (b) Misfit as a function of slip rate and dip angle of the ramp of the ramp-décollement model. Purple and orange stars mark the best-fitting south-dipping and north-dipping model, respectively, and dashed lines are the 70 % and 90 % confidence contours. The width of the ramp is estimated to be ~96 km. (c) Misfit as a function of the distance to the north of the East Kunlun fault (with the other parameters fixed at the optimal values). Purple and orange stars and error bars indicate the best-fitting positions and 70 % confidence intervals, respectively. (d) Observed (blue vectors) and model-predicted (red vectors) uplift rates. (e) Observed (blue vectors) and modeled (red vectors) horizontal velocities. In (d) and (e), error bars and error ellipses represent the 39.5 % and 95 % confidence level, respectively. In (e), purple and orange solid lines mark the surface trace of the best-fitting south-dipping ramp and north-dipping ramp, respectively; purple and orange dashed lines indicate the 70 % confidence interval; black dashed line marks the position of profile in (a) and (c); the abbreviation KPF stands for the Kunlun Pass fault.

unrealistically high, as no surface geomorphological evidence in this arid region has been found to support sustained tectonic activity along the NKT. While the presence of a blind thrust system (Karplus et al., 2019) cannot be excluded, the long-term slip rate of such a blind fault system would need to be below the sedimentation rate of <0.5 mm/yr along the basin margin (Métivier et al., 1999). Nonetheless, we cannot completely rule out the roles of unidentified thrust faults and structures, given the geological complexity of this region and the limited access due to harsh environmental conditions.

Another possible explanation is the vertical uplift adjacent to the sub-vertical East Kunlun fault (EKF) system (e.g., Lasserre et al., 2005) with transpressional structures such as fault junctions and restraining bends (e.g., Duvall et al., 2013; Staisch et al., 2020). One of the fault junctions crossed by our GPS profile (Fig. 6e) manifests itself as a

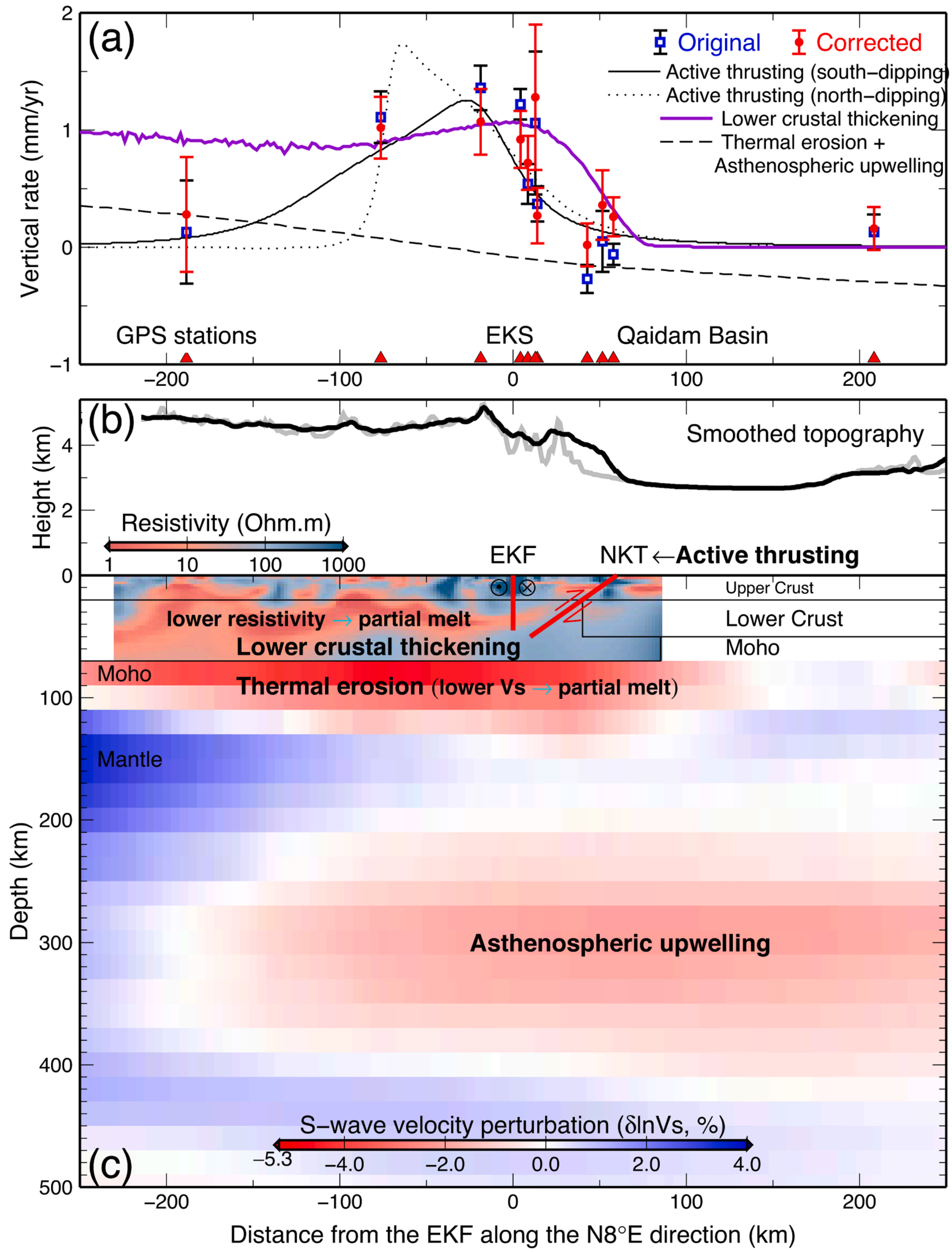

Fig. 7. Interpretation of the observed uplift rate: (a) Original (blue squares) and corrected (red dots) vertical GPS rates and model predictions (solid, dotted, and dashed lines) for the four physical processes labeled. Red bars indicate the combined GPS and model-prediction (for the isostatic adjustment in Fig. 4c-4f) 1-sigma uncertainties. (b) Topography in center (gray line) and smoothed over 100-km-wide swath of the cyan rectangle in Fig. 2a. (c) Physical processes: (1) Active thrusting on the possible North Kunlun thrust fault, (2) lower crustal thickening south of the Qaidam Basin, (3) thermal erosion below the Moho, and (4) asthenospheric upwelling. Also shown are magnetotelluric crustal resistivity results (Le Pape et al., 2012) and mantle shear wave velocity (Vs) perturbations from seismic tomography (Chen et al., 2017b).

junction of the S82°E-striking Kusai Lake segment of the EKF, its eastward continuation along the N87°E-striking Xidatan segment, and the about 100-km-long and S82°E-striking Kunlun Pass fault (KPF). How the EKF connects with the KPF at depth remains unknown, as the KPF may be either a branch sinistral–reverse fault that merges with the EKF at depth or a separated sinistral–reverse fault dipping toward the north (Duvall et al., 2013). Nonetheless, because the KPF is within 30 km off the EKF and slips left laterally at a rate of only about 1 mm/yr (Wang et al., 2013), fault activity on this fault junction system cannot produce an active uplift of 1–2 mm/yr that extends about 100 km southward of the EKF. Furthermore, fault activity along the small restraining bends along the EKF (longitude 93°E-96°E) drives localized uplift adjacent to the fault trace (Staisch et al., 2020), which does not fit the GPS-observed long-wavelength uplift. Hence, we need to consider other physical processes to explain the GPS-derived uplift.

The candidate processes include geodynamic mantle processes that possibly have elevated the EKS since ~25 Ma (Ding et al., 2022), such as thermal erosion below the Moho and asthenospheric upwelling (Chen et al., 2017b; Rao and Sun, 2021) (Fig. 7c and Fig. S28-S31). However, the two processes would produce long-wavelength ongoing uplift across the EKS (Fig. 7a and Fig. S30-S31; Text S11), which is inconsistent with the sharp GPS-observed gradient. Also, both processes drive expansion near the EKS, which conflicts with GPS-derived contraction strain rate of about 2–5 × 10^{-9}/yr (Fig. 2a) (Wang and Shen, 2020; Wang and Barbot, 2023). Another alternative driving process resides in the lower crust (Clark et al., 2005; Le Pape et al., 2012), as the weaker lower crustal material from the plateau interior extrudes across the EKF (Le Pape et al., 2012) and might extend ~40 km beneath the Qaidam crust (Karplus et al., 2019), resulting in crustal thickening beneath the EKS (Fig. 1d and Fig. 7c).

To simulate lower-crustal thickening near the EKS in response to far-field loading, we use a 2D finite element model that accounts for the topographic variation and mechanically weaker lower crust beneath the plateau (Fig. 8). We consider a mafic granulite rheology for the lower crust beneath the high plateau, and the effective viscosity is about 5 × 10^{19}–5 × 10^{20} Pa s, which agrees with the upper bound obtained by modeling the decadal-scale interseismic deformation (Ge et al., 2022). Without the far-field loading to the lower crust (Fig. 8b), the plateau experiences gravitational collapse, but the region near the basin margin rises. As the far-field loading is turned on and persists for ~0.68 Ma, the uplift domain expands toward the plateau side, reaching ~100 km south of the EKF (Fig. 7 and Fig. 8c). To reproduce the observed uplift pattern, the far-field loading in the form of lateral lower-crust flow has to be about 10 mm/yr (Fig. S27), consistent with the results from a 3D plateau-scale simulation (Bischoff and Flesch, 2018), and the lower crustal material is transported at 1–2 mm/yr across the downdip extension of the EKF. The misfit to the observed uplift north of the EKF likely results from the absence of a rheological transition zone between the plateau and the basin in our 2D model (Fig. 8a). The misfit to the observed uplift about 200 km south of the EKF arises because our 2D

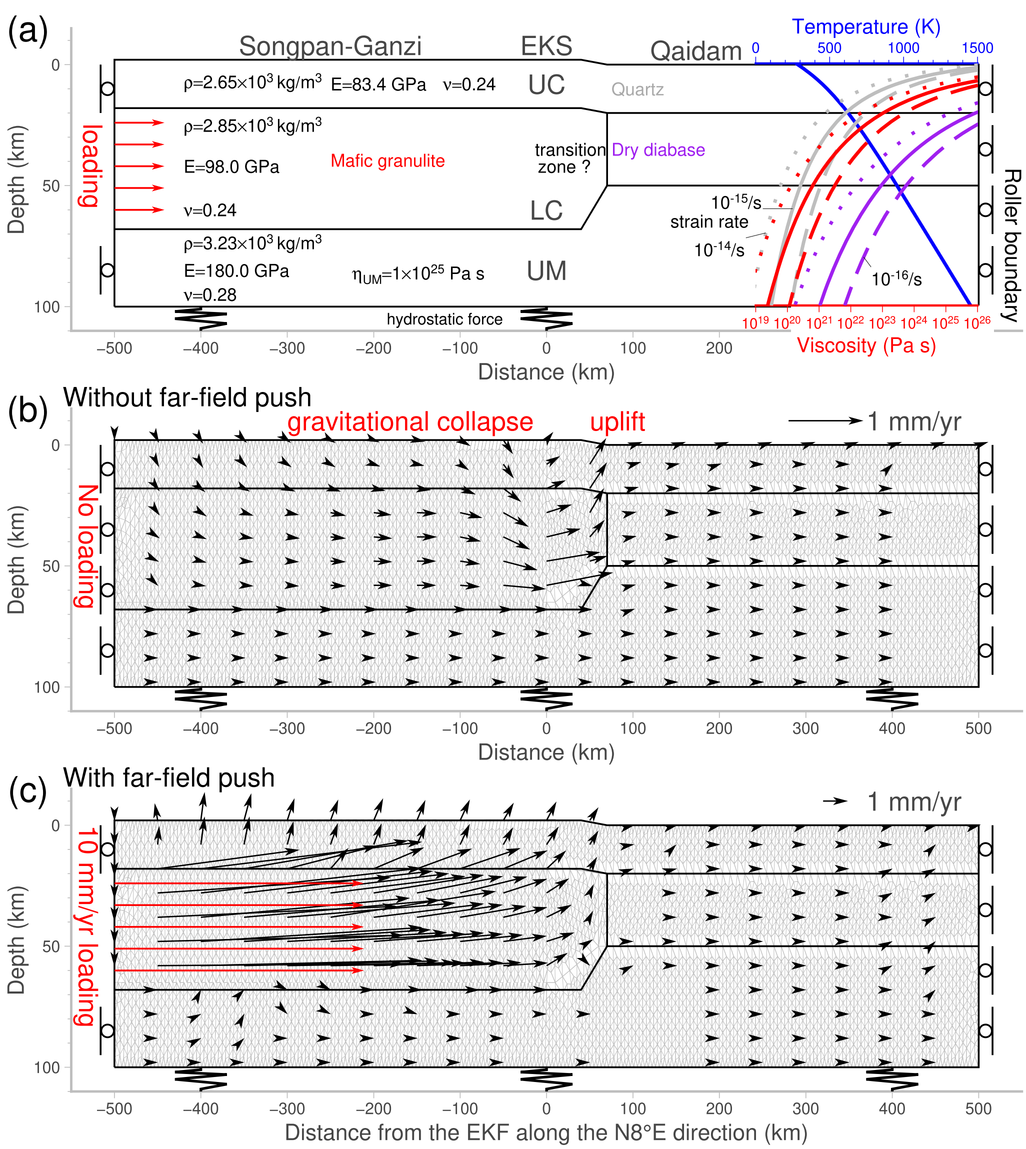

Fig. 8. 2D finite element model of lower crustal thickening. (a) Model geometry, boundary conditions, geotherm, and material properties. ρ is the density, E the Young's modulus, ν Poisson's ratio. Blue line indicates the background geotherm representative of this region. Gray, red, and purple lines indicate the effective viscosities of quartz-dominated (Carter and Tsenn, 1987), mafic granulite (Wang et al., 2012), and dry diabase (Mackwell et al., 1998) rocks, respectively, subjected to three loading strain rates (10^{-16}, 10^{-15}, and 10^{-14}/s for long dashed, solid, and dotted lines, respectively). (b) Velocity field (black vectors) for the simulation without far-field loading exerted to the left side of the lower crust. (c) Velocity field after about 0.2 Ma since the onset of full 10 mm/yr far-field loading at the epoch of 1.5 Ma. The velocity loading is 10 mm/yr on the left side of the lower crust. Abbreviations: UC=Upper Crust; LC==Lower Crust; UM=Upper Mantle.

model for the north-south cross-section does not incorporate the eastward extrusion of the high plateau, which tends to lower the plateau surface in the plateau interior. In our model, a low slip rate thrust fault (reverse slip rate lower than 0.5 mm/yr) tends to be developed to the south of the basin margin, as a passive response to the lower crustal thickening beneath the EKS (Fig. 8c). On the other hand, if the lower crust beneath the plateau and basin exhibits no rheological contrast, the model predicts uplift in the basin's interior (Fig. S27), which contradicts the GPS-observed pattern. Hence, our results suggest that lower crustal thickening beneath the EKS could drive the observed uplift across the EKS.

5.2. Lower-crustal 'flow' and growing plateau margins

In active collisional orogens, mountain belts are commonly formed when the hanging wall rocks are thrust over the footwall and exhumed via erosion. The driving force for this mountain building is the horizontal convergence of two crustal blocks, as seen in the Qilian Shan and Qimen Tagh Range in Northern Tibet (Fig. 1 and Fig. 2), where active upper crustal shortening occurs (Wang and Shen, 2020), as well as in the Himalayas (Fig. 1), where large-scale thrust fault systems (Kapp and DeCelles, 2019) are accommodating ~15–20 mm/yr of shortening rate (Wang and Shen, 2020), resulting in ~5 mm/yr of active uplift (Fu and Freymueller, 2012). However, active uplift in the presence of limited horizontal shortening across the plateau margins, as found across the northern (EKS) and eastern (Longmen Shan) (Wang and Shen, 2020; Wang et al., 2021) margins of the Tibetan Plateau (Fig. 1), contradicts this paradigm and is diagnostic of lower crustal thickening (Liu et al., 2014; Staisch et al., 2016; Bischoff and Flesch, 2018; Karplus et al., 2019; Wang et al., 2021), a process that is essentially consistent with the lower-crustal 'flow' model (Royden et al., 1997; Clark et al., 2005).

Space geodesy brings additional arguments to the lower-crustal 'flow' model (Bird, 1991; Royden et al., 1997; Clark et al., 2005). Without the contributions from space geodesy, the presence of partial melt and fluids in the lower crust south of the EKS, as revealed by reduced seismic velocity (Li et al., 2014) and decreased electrical resistivity (Le Pape et al., 2012), are only suggestive of the mobility of the lower crustal materials. These physical properties are not direct measure of the inferred rheology, and direct observations reflecting sustainable motions of the lower crustal materials are required for a better understanding of the deforming system. Our GPS measurements, on the other hand, illustrate active uplift across the EKS that is likely linked with the deforming lower crust. The observed present-day uplift rates are well reproduced by the lower-crustal 'flow' model: weaker lower crustal materials (Le Pape et al., 2012; Li et al., 2014), subjected to topography-related lateral pressure and the far-field push from the Indian plate (Bischoff and Flesch, 2018), extrude across the EKF and produce the observed uplift. The success of this model may indicate that the lower-crustal 'flow' model applies to the active deformation across the EKS, a tectonic anomaly in Northern Tibet in which otherwise upper crustal shortening dominates.

6. Conclusions

We consider the climate-related surface processes and tectonic/geodynamic processes to interpret the GPS-observed uplift of 1–2 mm/yr on the EKS relative to the Qaidam Basin, in the context of limited shortening rate of at most 1 mm/yr. The GPS-observed uplift cannot be attributed to the isostatic response to surface processes and the post-seismic transients of the 2001 Mw7.8 Kokoxili event. Interseismic slip on thrust faults is unlikely to account for the GPS-observed uplift, as the reverse-slip rate required would be too large, and no active range-front fault has been identified. Mantle processes also fail to explain the sharp uplift gradient observed by GPS. In contrast, the rates and patterns of GPS-observed uplift and shortening across the East Kunlun Shan (EKS) support the hypothesis that lower crustal thickening is actively occurring beneath the EKS. In the absence of an identified blind thrust fault slipping at a rate greater than 1 mm/yr, our study demonstrates that lower crustal thickening remains the most plausible and physically consistent model.

CRediT authorship contribution statement

Shaozhuo Liu: Writing – review & editing, Writing – original draft, Visualization, Validation, Software, Resources, Methodology, Investigation, Formal analysis, Data curation, Conceptualization. **Xiwei Xu:** Writing – review & editing, Project administration, Funding acquisition, Formal analysis, Data curation. **Jean-Mathieu Nocquet:** Writing – review & editing, Investigation, Formal analysis, Data curation. **Guihua Chen:** Writing – review & editing, Funding acquisition, Formal analysis, Data curation. **Xibin Tan:** Writing – review & editing, Formal analysis. **Sigurjón Jónsson:** Writing – review & editing, Funding acquisition, Formal analysis. **Yann Klinger:** Writing – review & editing, Resources, Project administration, Funding acquisition, Formal analysis, Data curation.

Declaration of competing interest

The authors declare that they have no known competing financial interests or personal relationships that could have appeared to influence the work reported in this paper.

Acknowledgments

We thank Jeffrey Freymueller and Andrew Zuza for constructive comments that improve this work. We thank Paul Tapponnier for inspiring discussions that eventually led to the Xidatan project. Liu appreciates the support of K.C.Wong Education Foundation, Hong Kong and CNRS. Liu benefitted from discussions with Prof. Zheng-Kang Shen, Dr. Jiankun He, Liangyu Zhu, Yujiang Li, Shangxin Liu, Michael Pons, Xiangjiang Yu, Xiangke Xu, Guoqing Zhang, and Qing Yan. Liu thanks Prof. Chéry for sharing the ADELI code; Dr. Le Page for sharing the MT results; and Dr. Rizheng He for sharing his Moho model. This work was supported by the National Natural Science Foundation of China (41941016 to X.X.), National Key Research and Development Project of China (2018YFC1504104 to X.X.), KAUST award BAS/1/1353–01–01 (to S.J.), ANR project ANR-005-CATT-0006 (to Y.K.), National Natural Science Foundation of China (40802052 to C.G. and U2139201 to S.L.), and CNRS-K.C.Wong Education Foundation (to S.L.).

Supplementary materials

Supplementary material associated with this article can be found, in the online version, at doi:10.1016/j.epsl.2025.119245.

Data availability

Data will be made available on request.

References

Aagaard, B.T., Knepley, M.G., Williams, C.A., 2013. A domain decomposition approach to implementing fault slip in finite-element models of quasi-static and dynamic crustal deformation. J. Geophys. Res. Solid Earth 118, 3059–3079.

Altamimi, Z., Rebischung, P., Métivier, L., Collilieux, X., 2016. ITRF2014: a new release of the International Terrestrial Reference Frame modeling nonlinear station motions. J. Geophys. Res. Solid Earth 121, 6109–6131.

Armijo, R., Tapponnier, P., Mercier, J.L., Han, T.-L., 1986. Quaternary extension in southern Tibet: field observations and tectonic implications. J. Geophys. Res. Solid Earth 91, 13803–13872.

Barbot, S., Fialko, Y., Bock, Y., 2009. Postseismic deformation due to the Mw 6.0 2004 Parkfield earthquake: stress-driven creep on a fault with spatially variable rate-and-state friction parameters. J. Geophys. Res. Solid Earth 114, B07405.

Bird, P., 1991. Lateral extrusion of lower crust from under high topography in the isostatic limit. J. Geophys. Res. Solid Earth 96, 10275–10286.

Bischoff, S.H., Flesch, L.M., 2018. Normal faulting and viscous buckling in the Tibetan Plateau induced by a weak lower crust. Nat. Commun. 9, 4952.
Blisniuk, P.M., Hacker, B.R., Glodny, J., Ratschbacher, L., Bi, S., Wu, Z., McWilliams, M. O., Calvert, A., 2001. Normal faulting in central Tibet since at least 13.5 myr ago. Nature 412, 628–632.
Carter, N.L., Tsenn, M.C., 1987. Flow properties of continental lithosphere. Tectonophysics. 136, 27–63.
Chen, J.Y., Pan, E., Bevis, M., 2017a. Accurate computation of the elastic load love numbers to high spectral degree for a finely layered, transversely isotropic and self-gravitating Earth. Geophys. J. Int. 212, 827–838.
Chen, M., Niu, F., Tromp, J., Lenardic, A., Lee, C.-T.A., Cao, W., Ribeiro, J., 2017b. Lithospheric foundering and underthrusting imaged beneath Tibet. Nat. Commun. 8, 15659.
Clark, M.K., Bush, J.W.M., Royden, L.H., 2005. Dynamic topography produced by lower crustal flow against rheological strength heterogeneities bordering the Tibetan Plateau. Geophys. J. Int. 162, 575–590.
Clark, M.K., Farley, K.A., Zheng, D., Wang, Z., Duvall, A.R., 2010. Early Cenozoic faulting of the northern Tibetan Plateau margin from apatite (U–Th)/He ages. Earth Planet. Sci. Lett. 296, 78–88.
Dill, R., Dobslaw, H., 2013. Numerical simulations of global-scale high-resolution hydrological crustal deformations. J. Geophys. Res. Solid Earth 118, 5008–5017.
Ding, L., Kapp, P., Cai, F., Garzione, C.N., Xiong, Z., Wang, H., Wang, C., 2022. Timing and mechanisms of Tibetan Plateau uplift. Nature Rev. Earth & Environ. 3, 652–667.
Döll, P., Müller Schmied, H., Schuh, C., Portmann, F.T., Eicker, A., 2014. Global-scale assessment of groundwater depletion and related groundwater abstractions: combining hydrological modeling with information from well observations and GRACE satellites. Water. Resour. Res. 50, 5698–5720.
Duvall, A.R., Clark, M.K., Kirby, E., Farley, K.A., Craddock, W.H., Li, C., Yuan, D.-Y., 2013. Low-temperature thermochronometry along the Kunlun and Haiyuan Faults, NE Tibetan Plateau: evidence for kinematic change during late-stage orogenesis. Tectonics. 32, 1190–1211.
Dziewonski, A.M., Anderson, D.L., 1981. Preliminary reference Earth model. Phys. Earth and Planetary Interiors 25, 297–356.
Elliott, J.R., Walters, R.J., England, P.C., Jackson, J.A., Li, Z., Parsons, B., 2010. Extension on the Tibetan plateau: recent normal faulting measured by InSAR and body wave seismology. Geophys. J. Int. 183, 503–535.
England, P.C., Houseman, G.A., 1988. The mechanics of the Tibetan Plateau. Philosophical Trans. Royal Soc. London. Series A, Mathemat. Phys. Sci. 326, 301–320.
Euen, G.T., Liu, S., Gassmöller, R., Heister, T., King, S.D., 2023. A comparison of 3-D spherical shell thermal convection results at low to moderate Rayleigh number using ASPECT (version 2.2.0) and CitcomS (version 3.3.1). Geosci. Model Dev. 16, 3221–3239.
Fan, Y., van den Dool, H., 2004. Climate Prediction Center global monthly soil moisture data set at 0.5° resolution for 1948 to present. J. Geophys. Res. Atmospheres 109, D10102.
Farrell, W.E., 1972. Deformation of the Earth by surface loads. Rev. Geophysics 10, 761–797.
Flament, N., Gurnis, M., Müller, R.D., 2013. A review of observations and models of dynamic topography. Lithosphere 5, 189–210.
Fu, Y., Freymueller, J.T., 2012. Seasonal and long-term vertical deformation in the Nepal Himalaya constrained by GPS and GRACE measurements. J. Geophys. Res. Solid Earth 117, B03407.
Ge, W.-P., Molnar, P., Shen, Z.-K., Li, Q., 2015. Present-day crustal thinning in the southern and northern Tibetan Plateau revealed by GPS measurements. Geophys. Res. Lett. 42, 5227–5235.
Ge, W.-P., Shen, Z.-K., Molnar, P., Wang, M., Zhang, P.-Z., Yuan, D.-Y., 2022. GPS determined asymmetric deformation across Central Altyn Tagh fault reveals rheological structure of Northern Tibet. J. Geophys. Res. Solid Earth 127, e2022JB024216.
Hammond, W.C., Blewitt, G., Kreemer, C., Nerem, R.S., 2021. GPS imaging of global vertical land motion for studies of sea level rise. J. Geophys. Res. Solid Earth 126, e2021JB022355.
Hassani, R., Jongmans, D., Chéry, J., 1997. Study of plate deformation and stress in subduction processes using two-dimensional numerical models. J. Geophys. Res. Solid Earth 102, 17951–17965.
Heister, T., Dannberg, J., Gassmöller, R., Bangerth, W., 2017. High accuracy mantle convection simulation through modern numerical methods – II: realistic models and problems. Geophys. J. Int. 210, 833–851.
Herring, T., King, R., Floyd, M., McClusky, S., 2017. Introduction to GAMIT/GLOBK, Release 10.7. Massachusetts Institute of Technology, Cambridge.
Hugonnet, R., McNabb, R., Berthier, E., Menounos, B., Nuth, C., Girod, L., Farinotti, D., Huss, M., Dussaillant, I., Brun, F., Kääb, A., 2021. Accelerated global glacier mass loss in the early twenty-first century. Nature 592, 726–731.
Jiang, G., Hu, S., Shi, Y., Zhang, C., Wang, Z., Hu, D., 2019. Terrestrial heat flow of continental China: updated dataset and tectonic implications. Tectonophysics. 753, 36–48.
Jolivet, M., Brunel, M., Seward, D., Xu, Z., Yang, J., Malavieille, J., Roger, F., Leyreloup, A., Arnaud, N., Wu, C., 2003. Neogene extension and volcanism in the Kunlun Fault Zone, northern Tibet: new constraints on the age of the Kunlun Fault. Tectonics. 22.
Jordan, T.A., Watts, A.B., 2005. Gravity anomalies, flexure and the elastic thickness structure of the India–Eurasia collisional system. Earth Planet. Sci. Lett. 236, 732–750.
Kapp, P., DeCelles, P.G., 2019. Mesozoic–Cenozoic geological evolution of the himalayan-tibetan orogen and working tectonic hypotheses. Am. J. Sci. 319, 159–254.
Karplus, M.S., Klemperer, S.L., Zhao, W., Kind, R., Wu, Z., Mechie, J., Shi, D., Brown, L. D., Chen, C., Su, H., Xue, G., Sandvol, E., Ni, J., Tilmann, F.J., Chen, Y.J., 2019. Receiver-function imaging of the lithosphere at the Kunlun-Qaidam boundary. Northeast Tibet. Tectonophys. 759, 30–43.
Karplus, M.S., Zhao, W., Klemperer, S.L., Wu, Z., Mechie, J., Shi, D., Brown, L.D., Chen, C., 2011. Injection of Tibetan crust beneath the south Qaidam Basin: evidence from INDEPTH IV wide-angle seismic data. J. Geophys. Res. Solid Earth 116, B07301.
Kronbichler, M., Heister, T., Bangerth, W., 2012. High accuracy mantle convection simulation through modern numerical methods. Geophys. J. Int. 191, 12–29.
Lasserre, C., Peltzer, G., Crampé, F., Klinger, Y., Van der Woerd, J., Tapponnier, P., 2005. Coseismic deformation of the 2001 Mw=7.8 Kokoxili earthquake in Tibet, measured by synthetic aperture radar interferometry. J. Geophys. Res. Solid Earth 110, B12408.
Lau, H.C.P., Austermann, J., Holtzman, B.K., Havlin, C., Lloyd, A.J., Book, C., Hopper, E., 2021. Frequency dependent mantle viscoelasticity via the complex viscosity: cases from Antarctica. J. Geophys. Res. Solid Earth 126, e2021JB022622.
Le Pape, F., Jones, A.G., Vozar, J., Wenbo, W., 2012. Penetration of crustal melt beyond the Kunlun Fault into northern Tibet. Nat. Geosci. 5, 330.
Lee, E., Carrivick, J.L., Quincey, D.J., Cook, S.J., James, W.H.M., Brown, L.E., 2021. Accelerated mass loss of Himalayan glaciers since the Little Ice Age. Sci. Rep. 11, 24284.
Li, C., Zheng, D., Zhou, R., Yu, J., Wang, Y., Pang, J., Wang, Y., Hao, Y., Li, Y., 2021. Late oligocene tectonic uplift of the East Kunlun Shan: expansion of the Northeastern Tibetan Plateau. Geophys. Res. Lett. 48, e2020GL091281.
Li, H., Shen, Y., Huang, Z., Li, X., Gong, M., Shi, D., Sandvol, E., Li, A., 2014. The distribution of the mid-to-lower crustal low-velocity zone beneath the northeastern Tibetan Plateau revealed from ambient noise tomography. J. Geophys. Res.: Solid Earth 119, 1954–1970.
Liu, G., Zhang, X., Cui, Z., Wu, Y., Ju, Y., 2006. A review of glacial sequences of the Kunlun Pass, northern Tibetan Plateau. Quat. Int. 154-155, 63–72.
Liu, Q.Y., van der Hilst, R.D., Li, Y., Yao, H.J., Chen, J.H., Guo, B., Qi, S.H., Wang, J., Huang, H., Li, S.C., 2014. Eastward expansion of the Tibetan Plateau by crustal flow and strain partitioning across faults. Nat. Geosci. 7, 361–365.
Liu, S., King, S.D., 2019. A benchmark study of incompressible stokes flow in a 3-D spherical shell using ASPECT. Geophys. J. Int. 217, 650–667.
Liu, S., King, S.D., 2022. Dynamics of the North American plate: large-scale driving mechanism from far-field slabs and the interpretation of shallow negative seismic anomalies. Geochemistry, Geophysics, Geosystems 23, e2021GC009808.
Liu, S., Moulin, A., Jónsson, S., 2024. Unloading uplift caused by surface processes in New Zealand's Southern Alps. Geophys. Res. Lett. 51, e2024GL109019.
Liu, S., Xu, X., Klinger, Y., Nocquet, J.-M., Chen, G., Yu, G., Jónsson, S., 2019. Lower crustal heterogeneity beneath the Northern Tibetan plateau constrained by GPS measurements following the 2001 Mw7.8 Kokoxili earthquake. J. Geophys. Res.: Solid Earth 124, 11992–12022.
Mackwell, S.J., Zimmerman, M.E., Kohlstedt, D.L., 1998. High-temperature deformation of dry diabase with application to tectonics on Venus. Journal of Geophysical Research: Solid Earth 103, 975–984.
Melini, D., Saliby, C., Spada, G., 2022. On computing viscoelastic love numbers for general planetary models: the ALMA3 code. Geophys. J. Int. 231, 1502–1517.
Métivier, F., Gaudemer, Y., Tapponnier, P., Klein, M., 1999. Mass accumulation rates in Asia during the cenozoic. Geophys. J. Int. 137, 280–318.
Molnar, P., England, P., Martinod, J., 1993. Mantle dynamics, uplift of the Tibetan Plateau, and the Indian Monsoon. Rev. Geophys. 31, 357–396.
Okada, Y., 1992. Internal deformation due to shear and tensile faults in a half-space. Bulletin Seismol. Soc. America 82, 1018–1040.
Owen, L.A., 2009. Latest pleistocene and holocene glacier fluctuations in the Himalaya and Tibet. Quat. Sci. Rev. 28, 2150–2164.
Rao, W., Sun, W., 2021. Moho interface changes beneath the Tibetan plateau based on GRACE data. J. Geophys. Res.: Solid Earth 126, e2020JB020605.
Royden, L.H., Burchfiel, B.C., King, R.W., Wang, E., Chen, Z., Shen, F., Liu, Y., 1997. Surface deformation and lower crustal flow in eastern Tibet. Science (1979) 276, 788–790.
Royden, L.H., Burchfiel, B.C., van der Hilst, R.D., 2008. The geological evolution of the Tibetan Plateau. Science (1979) 321, 1054–1058.
Ryder, I., Bürgmann, R., Pollitz, F., 2011. Lower crustal relaxation beneath the Tibetan Plateau and Qaidam Basin following the 2001 Kokoxili earthquake. Geophys. J. Int. 187, 613–630.
Shapiro, N.M., Ritzwoller, M.H., Molnar, P., Levin, V., 2004. Thinning and flow of Tibetan crust constrained by seismic anisotropy. Science (1979) 305, 233–236.
Shen, Z.K., Wang, M., Zeng, Y., Wang, F., 2015. Optimal interpolation of spatially discretized geodetic DataOptimal interpolation of spatially discretized geodetic data. Bullet. Seismolog. Soc. America 105, 2117–2127.
Shi, D., Shen, Y., Zhao, W., Li, A., 2009. Seismic evidence for a Moho offset and south-directed thrust at the easternmost Qaidam–Kunlun boundary in the Northeast Tibetan plateau. Earth Planet. Sci. Lett. 288, 329–334.
Spada, G., Barletta, V.R., Klemann, V., Riva, R.E.M., Martinec, Z., Gasperini, P., Lund, B., Wolf, D., Vermeersen, L.L.A., King, M.A., 2011. A benchmark study for glacial isostatic adjustment codes. Geophys. J. Int. 185, 106–132.
Staisch, L.M., Niemi, N.A., Clark, M.K., Chang, H., 2016. Eocene to late oligocene history of crustal shortening within the Hoh Xil Basin and implications for the uplift history of the northern Tibetan Plateau. Tectonics. 35, 862–895.

Staisch, L.M., Niemi, N.A., Clark, M.K., Chang, H., 2020. The cenozoic evolution of crustal shortening and left-lateral shear in the Central East Kunlun Shan: implications for the uplift history of the Tibetan plateau. Tectonics. 39, e2020TC006065.
Styron, R., Taylor, M., Sundell, K., 2015. Accelerated extension of Tibet linked to the northward underthrusting of Indian crust. Nat. Geosci. 8, 131.
Tapponnier, P., Xu, Z., Roger, F., Meyer, B., Arnaud, N., Wittlinger, G., Yang, J., 2001. Oblique stepwise rise and growth of the Tibet plateau. Science (1979) 294, 1671–1677.
Taylor, M., Yin, A., Ryerson, F.J., Kapp, P., Ding, L., 2003. Conjugate strike-slip faulting along the Bangong-Nujiang suture zone accommodates coeval east-west extension and north-south shortening in the interior of the Tibetan Plateau. Tectonics. 22, 1044.
Van der Woerd, J., Ryerson, F.J., Tapponnier, P., Gaudemer, Y., Finkel, R., Meriaux, A.S., Caffee, M., Zhao, G., He, Q., 1998. Holocene left-slip rate determined by cosmogenic surface dating on the Xidatan segment of the Kunlun fault (Qinghai, China). Geology. 26, 695–698.
Wang, C., Gao, R., Yin, A., Wang, H., Zhang, Y., Guo, T., Li, Q., Li, Y., 2011. A mid-crustal strain-transfer model for continental deformation: a new perspective from high-resolution deep seismic-reflection profiling across NE Tibet. Earth Planet. Sci. Lett. 306, 279–288.
Wang, L., Barbot, S., 2023. Three-dimensional kinematics of the India–Eurasia collision. Commun. Earth. Environ. 4, 164.
Wang, M., Shen, Z.-K., 2020. Present-day crustal deformation of continental China derived from GPS and its tectonic implications. J. Geophys. Res. Solid Earth 125, e2019JB018774.
Wang, M., Shen, Z.-K., Wang, Y.-Z., Bürgmann, R., Wang, F., Zhang, P.-Z., Liao, H., Zhang, R., Wang, Q., Jiang, Z.-S., Chen, W.-T., Hao, M., Li, Y., Gu, T., Tao, W., Wang, K., Xue, L., 2021. Postseismic deformation of the 2008 Wenchuan Earthquake illuminates lithospheric rheological structure and dynamics of Eastern Tibet. J. Geophys. Res. Solid Earth 126, e2021JB022399.
Wang, Y., Wang, M., Shen, Z.-K., Ge, W., Wang, K., Wang, F., Sun, J., 2013. Inter-seismic deformation field of the Ganzi-Yushu fault before the 2010 Mw 6.9 Yushu earthquake. Tectonophysics. 584, 138–143.
Wang, Y.F., Zhang, J.F., Jin, Z.M., Green, H.W., 2012. Mafic granulite rheology: implications for a weak continental lower crust. Earth Planet. Sci. Lett. 353-354, 99–107.
Watts, A.B., Zhong, S.J., Hunter, J., 2013. The behavior of the lithosphere on seismic to geologic timescales. Annu Rev. Earth. Planet. Sci. 41, 443–468.
Wen, Y., Li, Z., Xu, C., Ryder, I., Bürgmann, R., 2012. Postseismic motion after the 2001 MW 7.8 Kokoxili earthquake in Tibet observed by InSAR time series. J. Geophys. Res. Solid Earth 117, B08405.
Wu, C., Zuza, A.V., Chen, X., Ding, L., Levy, D.A., Liu, C., Liu, W., Jiang, T., Stockli, D.F., 2019. Tectonics of the Eastern Kunlun Range: cenozoic reactivation of a paleozoic-early mesozoic orogen. Tectonics. 38, 1609–1650.
Xu, X., Yi, C., 2014. Little Ice age on the Tibetan Plateau and its bordering mountains: evidence from moraine chronologies. Glob. Planet. Change 116, 41–53.
Yan, Q., Owen, L.A., Wang, H., Zhang, Z., 2018. Climate constraints on glaciation over high-mountain Asia during the last glacial maximum. Geophys. Res. Lett. 45, 9024–9033.
Yan, Q., Owen, L.A., Zhang, Z., Jiang, N., Zhang, R., 2020. Deciphering the evolution and forcing mechanisms of glaciation over the Himalayan-Tibetan orogen during the past 20,000 years. Earth Planet. Sci. Lett. 541, 116295.
Yin, A., Dang, Y.-Q., Zhang, M., Chen, X.-H., McRivette, M.W., 2008. Cenozoic tectonic evolution of the Qaidam basin and its surrounding regions (Part 3): structural geology, sedimentation, and regional tectonic reconstruction. GSA Bulletin 120, 847–876.
Yin, A., Harrison, T.M., 2000. Geologic evolution of the himalayan-tibetan orogen. Annu Rev. Earth. Planet. Sci. 28, 211–280.
Zhang, G., Yao, T., Shum, C.K., Yi, S., Yang, K., Xie, H., Feng, W., Bolch, T., Wang, L., Behrangi, A., Zhang, H., Wang, W., Xiang, Y., Yu, J., 2017. Lake volume and groundwater storage variations in Tibetan Plateau's endorheic basin. Geophys. Res. Lett. 44, 5550–5560.
Zhao, D., Qu, C., Bürgmann, R., Gong, W., Shan, X., 2021. Relaxation of Tibetan lower crust and afterslip driven by the 2001 Mw7.8 Kokoxili, China, earthquake constrained by a decade of geodetic measurements. Journal of Geophysical Research: Solid Earth 126, e2020JB021314.